# Spin dynamics of electrons and holes in InGaAs/GaAs quantum wells at millikelvin temperatures

L. V. Fokina,[1] I. A. Yugova,[2] D. R. Yakovlev,[1,3] M. M. Glazov,[3] I. A. Akimov,[1,3] A. Greilich,[1] D. Reuter,[4]
A. D. Wieck,[4] and M. Bayer[1]

[1]*Experimentelle Physik II, Technische Universität Dortmund, D-44221 Dortmund, Germany*
[2]*Department of Solid State Physics, Physical Faculty, St. Petersburg State University, 198504 St. Petersburg, Russia*
[3]*Ioffe Physical-Technical Institute, Russian Academy of Sciences, 194021 St. Petersburg, Russia*
[4]*Angewandte Festkörperphysik, Ruhr-Universität Bochum, D-44780 Bochum, Germany*

The carrier spin dynamics in a $n$-doped (In,Ga)As/GaAs quantum well has been studied by time-resolved Faraday rotation and ellipticity techniques in the temperature range down to 430 milliKelvin. These techniques give data with very different spectral dependencies, from which nonetheless consistent information on the spin dynamics can be obtained, in agreement with theoretical predictions. The mechanisms of long-lived spin coherence generation are discussed for the cases of trion and exciton resonant excitation. We demonstrate that carrier localization leads to a saturation of spin relaxation times at 45 ns for electrons below 4.5 K and at 2 ns for holes below 2.3 K. The underlying spin relaxation mechanisms are discussed.

PACS number(s): 78.67.De, 78.47.−p, 71.35.−y

## I. INTRODUCTION

The spin physics of semiconductor heterostructures attracts considerable attention nowadays due to the emerging fields of semiconductor spintronics, quantum computation, and quantum information.[1–3] Understanding the basic mechanisms providing spin orientation, spin relaxation, and spin decoherence of electrons and holes as well as manifestation of these mechanisms in various experimental conditions, e.g., external magnetic fields, lattice temperatures, etc., is of great importance in this respect. One of the evident goals is to optimize material properties and heterostructure design to achieve the longest possible spin relaxation time so that sufficient room is left for implementing protocols for spin manipulation and read out.

Carrier localization quenches the particle orbital motion and is one of the pathways to suppress efficient spin relaxation mechanisms related to the spin-orbit interaction. It has been shown that the spin relaxation time of electrons localized on donors in bulk GaAs can exceed 100 ns.[4,5] Also in (In,Ga)As/GaAs quantum dots the electron spin coherence time can reach 3 $\mu$s, while the hole spin relaxation time may exceed tens of nanoseconds.[6,7] In quantum well structures localization of the two-dimensional electrons at liquid helium temperatures is required to demonstrate relaxation times in the order of tens of nanoseconds.[8,9] Under these conditions spin relaxation times of few nanoseconds have been reported for resident holes.[10–13] Very recently a remarkably long hole spin relaxation time of 70 ns has been measured at 400 mK by a resonant spin amplification technique in $p$-doped GaAs/(Al,Ga)As quantum wells.[14] This time decreases to 2.5 ns with the temperature increase up to 4.5 K. Evidently temperatures below those that can be obtained by pumping $^4$He (about 1.5 K) are essential for understanding the carrier spin dynamics in quantum wells. However, the available experimental data are very limited in this range, mostly due to the demanding efforts for performing experiments with $^3$He and the complicated direct optical access to the sample in this case.

In this paper, we apply time-resolved Faraday rotation (FR) and ellipticity techniques to study the carrier spin dynamics in $n$-doped (In,Ga)As/GaAs quantum well. In Sec. II, we provide a description of these pump-probe techniques. Experimental features and theoretical modeling of the detected spin polarization are discussed in Sec. III. Two contributions to the Faraday rotation and ellipticity signals due to interaction of the probe beam with the trion and exciton resonances are considered. In Sec. IV, we discuss the resident electron spin orientation by the circularly polarized pump. Two mechanisms are suggested for the initialization of the experimentally observed long-lived spin dynamics. In Sec. V, we focus on the long-lived spin dynamics of resident electrons measured in the regime of resonant spin amplification (RSA) at very low temperatures down to 430 mK. The characteristic batlike shape of the RSA signal contains information on the hole spin dynamics, which persists remarkably long at low temperatures. We discuss the mechanisms responsible for electron and hole spin relaxation in the addressed temperature ranges.

## II. EXPERIMENTAL DETAILS

We study a heterostructure with two coupled 8-nm-thick In$_{0.09}$Ga$_{0.91}$As/GaAs quantum wells (QWs) separated by a thin (1.7 nm) GaAs barrier. The layer sequence was grown on an undoped GaAs substrate with (100) orientation by molecular-beam epitaxy. It contains a 100 nm $n$-doped GaAs buffer layer separated by a 100 nm GaAs spacer from the QWs. The doped layer serves as source of resident electrons for the QWs. The two-dimensional electron gas density in the QWs does not exceed $10^{10}$ cm$^{-2}$ in absence of optical excitation. This structure was selected on purpose because of pronounced carrier localization at cryogenic temperatures.[9] The structure was optically characterized measuring the photoluminescence (PL) spectra [Fig. 1(a)]. In the PL spectrum two emission lines separated by 1.4 meV are observed which we attribute to exciton (X) and negatively charged trion (T) recombination.[9] Their full width at half maximum of 1 meV
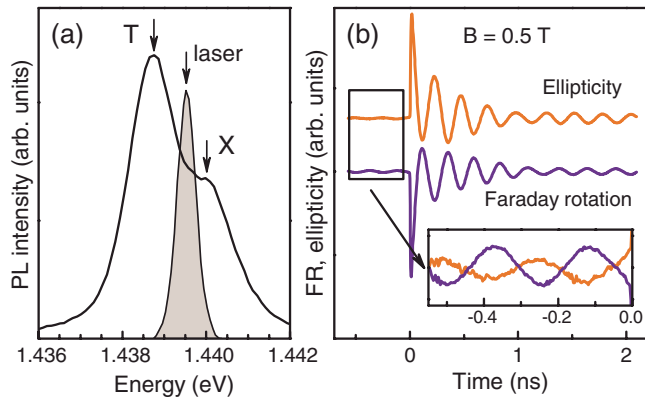
FIG. 1. (Color online) (a) Photoluminescence spectrum of the (In,Ga)As/GaAs QWs studied experimentally (black line). Filled contour represents the spectrum of the excitation laser used in the Faraday rotation and ellipticity experiments. (b) Time-resolved Faraday rotation and ellipticity signals measured in nondegenerate regime (pump at 1.4395 eV, probe at 1.4382 eV). Signals are vertically shifted for clarity. $T$=1.6 K. Inset: long-lived parts of the signals shortly before pump pulse arrival.

is caused by trion and exciton localization on alloy and QW width fluctuations.

In our pump-probe setup, we used one (degenerate regime) or two (nondegenerate regime) synchronized Ti:Sapphire lasers, each with pulse duration of 1.5 ps and pulse repetition period of 13.2 ns corresponding to a repetition frequency of 75.6 MHz. The laser wavelength was tuned in resonance with either the QW exciton or trion transitions. The circular polarization of the pump beam was modulated at 50 kHz by an elasto-optical modulator. The excitation density was kept close to the lowest possible limit at 0.5 W/cm². A sensitive balanced photodiode scheme was used for recording the Faraday rotation and ellipticity signals. Typical Faraday rotation or ellipticity angles in our experiments are on the order of 1.4 mrad. (The minimum detection angle is on the order of 0.8 $\mu$rad.) The sample was mounted in a cryostat with a split-coil superconducting magnet which allowed us to perform experiments in the Voigt configuration with the magnetic field **B**∥**x** oriented in the quantum well plane perpendicular to the light propagation direction (coinciding with the structure growth axis, denoted as $z$ axis). The sample temperature was varied from 0.34 to 80 K. For milliKelvin measurements the cryostat had a ³He insert, instead of a ⁴He variable temperature insert. The sample was then in contact with ³He in the insert, whose temperature could be changed between 0.34 and 100 K. Windows on the ³He insert allow direct optical access to the sample. When using this milliKelvin insert we tried to minimize the laser power as much as possible to avoid overheating of the sample. For the used excitation density of 0.5 W/cm², switching on the laser cases only weak increase in the bath temperature from 0.34 to 0.43 K. An increase in the excitation density by two-three times does not lead to visible changes in PL spectrum (namely, intensity ratio between the trion and exciton lines) and in the measured carrier spin dynamics. Therefore, we believe that the temperatures of the resident electrons, excitons, and trions do not deviate much from the bath temperature.

## III. DETECTION OF FARADAY ROTATION AND ELLIPTICITY SIGNALS

Figure 1(b) shows Faraday rotation and ellipticity signals obtained in the nondegenerate regime at $B$=0.5 T. The pump energy was approximately tuned to the exciton resonance and the signal was probed at a different energy close to the trion resonance. The Faraday rotation and ellipticity signals are similar to each other and contain a fast decaying part with a decay time of 360 ps, which is the typical recombination time for excitons and trions in these QWs. Therefore, we assign this component to the spin dynamics of photogenerated carriers.[15,16] Additionally a long-lived component can be seen at times exceeding 1 ns, which is even found at delays of about 13 ns, i.e., shortly before the next pump pulse arrival, as shown in the inset of Fig. 1(b). The long-lived signal is caused by generation of spin coherence for the resident electrons and its decay is solely controlled by the electron spin dephasing time, which may be as long as 55 ns in the studied structure.[9]

The scenarios of spin coherence generation for the resident electrons in quantum wells have been considered in Ref. 16. As a rule, the spin orientation of resident carriers involves either direct trion formation or trion formation from a spin oriented exciton generated by the pump. The trion formation is accompanied by capture of a resident electron with defined spin orientation, which results in polarization of the resident electron ensemble. Another mechanism can become involved for exciton excitation: due to the exchange scattering between a resident electron and the electron from a photocreated exciton the resident carriers can become spin polarized. We demonstrate below in Sec. IV that these two mechanisms can be equally important under resonant exciton excitation.

Now we turn to the spectral dependencies of the long-lived oscillations in the Faraday rotation and ellipticity signals, which are shown in Fig. 2. The experimental data measured at relatively large positive pump-probe delay of 2 ns and a small negative delay (shortly before pump pule arrival) are given in panels (a) and (b), respectively. The Faraday rotation and ellipticity signals obviously demonstrate quite different spectral behaviors. The maximum of the ellipticity signal and the zero of the FR signal are close to the trion resonance energy. Also, there is an extra feature in the ellipticity signal around the exciton resonance. Note that the spectral dependences of the FR and ellipticity signals measured for the pump tuned to the vicinity of the trion and exciton resonances show minor effect of the pump spectral positions (shift to low energies within the linewidth of trion resonance). Therefore, in Fig. 2 we present only results for the case where pump laser is resonant with the exciton energy.

The Faraday rotation, $\mathcal{F}$, and ellipticity, $\mathcal{E}$, of the probe pulse are proportional to the imaginary and real parts of the difference of quantum well transmission coefficients for $\sigma^+$ and $\sigma^-$ polarizations, $t_\pm$, respectively. Taking into account that for the relatively thin quantum wells studied here $t_\pm = 1 + r_\pm$ where $r_\pm(\omega)$ are the corresponding quantum well reflection coefficients[16,17]
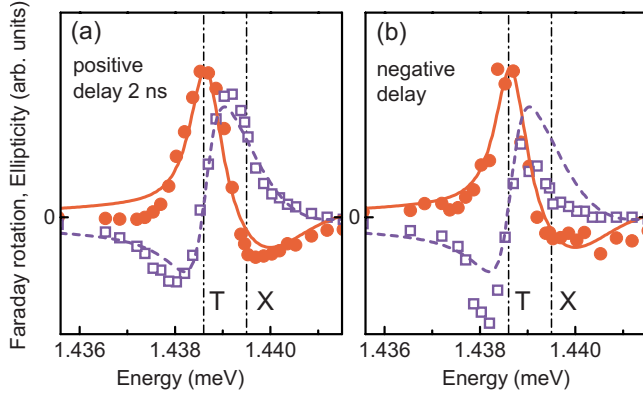
FIG. 2. (Color online) Dependencies of long-lived signal amplitudes of Faraday rotation (open squares and dashed lines) and ellipticity (closed circles and solid lines) on spectral position of probe. $B = 0.5$ T and $T = 1.6$ K. Experimental data are shown in panel (a) for a positive pump-probe delay of 2 ns and in panel (b) for a small negative delay. Pump at 1.4395 eV. Lines in both panels are fits by Eqs. (3) and (4) with the following parameters: $\hbar\Gamma_T = 0.65$ meV, $\hbar\bar{\Gamma}_X = 2.5$ meV, $\hbar\beta_X/\alpha_T = 1.56$ meV, $\hbar\omega_T = 1.4386$ eV, and $\hbar\omega_X = 1.4395$ eV. Dash-dot lines show exciton and trion energy positions obtained from the fit.

$$\mathcal{E} + i\mathcal{F} \propto r_+(\omega) - r_-(\omega). \tag{1}$$

Equation (1) is valid provided that $r_\pm(\omega) \ll 1$ which is the case for the studied system. The difference between $r_+$ and $r_-$ arises from the pump-induced spin polarization of the resident carriers. The quantum well reflection coefficients contain contributions from the X and T resonances:[18]

$$r_\pm(\omega) = \sum_{i=T,X} \frac{i\Gamma_{0,i}^\pm}{\omega_i^\pm - \omega - i(\Gamma_{0,i}^\pm + \Gamma_i^\pm)}. \tag{2}$$

Here $\omega_i^\pm$ are the resonance frequencies of exciton ($i = X$) and trion ($i = T$) for the corresponding circular polarizations, $\Gamma_{0,i}^\pm$ and $\Gamma_i^\pm$ are the radiative and nonradiative dampings, respectively (see Sec. 3.1.1 in Ref. 19).

When the spin-polarized resident electrons are probed by linearly polarized light different physical processes are responsible for the Faraday rotation and ellipticity signals, depending on whether the probe is resonant with either the trion or the exciton resonance. This is explained schematically in Fig. 3. The linearly polarized probe pulse can be decomposed into two circularly polarized components, one of which interacts with the spin-polarized resident electrons more efficiently compared with the other. Although the experiments have been performed in the transmission geometry, it is convenient to describe the FR and ellipticity signals in the framework of quantum well reflection coefficients because the reflectivity is directly proportional to the strength of the light interaction with quantum well.

For the trion resonance shown in Figs. 3(a) and 3(c), the main modulation contribution is caused by the trion radiative broadening $\Gamma_{0,T}^\pm$ (trion oscillator strength). The trion oscillator strength in the $\sigma^\pm$ polarizations is proportional to the number of electrons with $z$ spin component $\pm 1/2$, $N_\pm$. Hence, $\Gamma_{0,T}^\pm = \alpha_T\Gamma_{0,X}N_\pm$, where $\Gamma_{0,X}$ is the exciton radiative
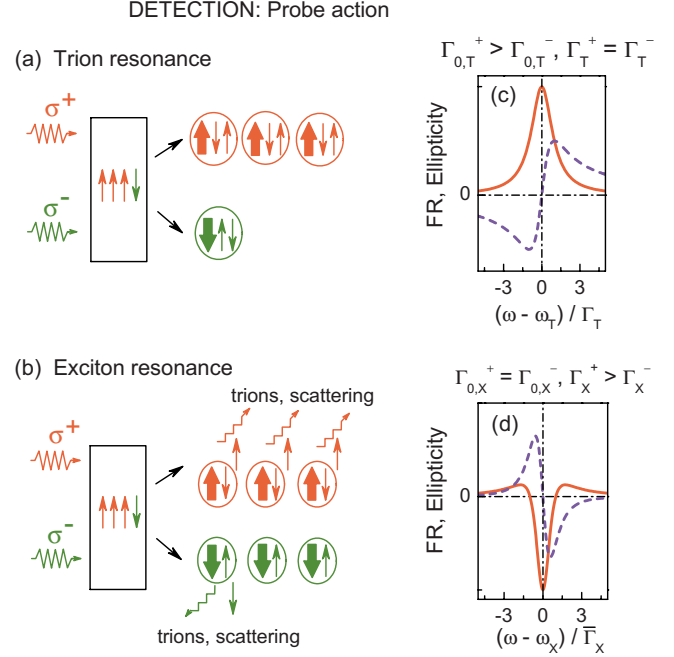


FIG. 3. (Color online) Schematic illustration of the Faraday rotation and ellipticity signal formation for probing the trion [panels (a) and (c)] and exciton [panels (b) and (d)] resonances. Thin arrows show electron spins, thick arrows show $z$ component of a photocreated hole spin. Broken lines marked by $\sigma^+$ and $\sigma^-$ show circular components of linearly polarized light. Thin arrows in the rectangle represent the polarized resident electron spins in quantum well. The numbers of trions shown by arrows in circles in panel (a) and excitons [panel (b)] represent the efficiency of the probe beam action on the QW with spin-polarized resident carriers. Broken lines marked by "trions, scattering" represent the decrease in exciton number due to exchange electron-exciton scattering and trion formation. Spectral dependences of Faraday rotation and ellipticity signals result from the imbalance of spin-up and spin-down resident electrons. They are shown in panels (c) and (d) by dashed and solid lines, correspondingly.

broadening calculated by neglecting electron spin polarization, and $\alpha_T$ is a constant related with the effective trion area, see Ref. 20. As a result, the difference of reflection coefficients in Eq. (1) takes the form

$$\mathcal{E} + i\mathcal{F} \propto \frac{i\alpha_T\Gamma_{0,X}(N_+ - N_-)}{\omega_T - \omega - i\Gamma_T}, \tag{3}$$

where we exploited the fact that the nonradiative broadening $\Gamma_T$ exceeds by far the radiative one, $\Gamma_{0,T}$. The corresponding shapes of the FR and ellipticity signals are shown in Fig. 3(c). The FR is an odd function of the detuning of the probe energy from the trion resonance, while the ellipticity is an even function.

For the exciton resonance shown in Figs. 3(b) and 3(d), the situation is different compared to the trion resonance. At low temperatures and in presence of spin-polarized resident electrons the dominant modulation effect results from the spin-dependent nonradiative damping of the excitons: $\Gamma_X^\pm = \bar{\Gamma}_X + \beta_X N_\pm$. Here $\bar{\Gamma}_X$ is the exciton nonradiative broaden-

ing, which does not depend on the exciton spin orientation. The spin-dependent part of the exciton broadening, $\beta_X N_\pm$, is caused by two processes: the exchange electron-exciton scattering and the trion formation by the photogenerated exciton and a spin-polarized resident electron, see Fig. 3(b). Here $\beta_X$ is a constant characterizing the efficiency of these spin-dependent mechanisms.[16,20] As a result the exciton contributions to the ellipticity and FR signals has the form

$$\mathcal{E} + i\mathcal{F} \propto -2\frac{\Gamma_{0,X}\beta_X(N_+ - N_-)}{(\omega_X - \omega - i\bar{\Gamma}_X)^2}, \qquad (4)$$

where we also neglected $\Gamma_{0,X}$ compared with $\bar{\Gamma}_X$. The corresponding exciton contributions to the FR and ellipticity signals are plotted in Fig. 3(d). The signs of the signals are inverted as compared with the trion case in Fig. 3(c). This is because for a given circular polarization the presence of spin-polarized electrons decreases the reflectivity in the vicinity of the exciton resonance, while the reflectivity at a trion resonance is enhanced.[20] The ellipticity signal has its minimum at the exciton resonance frequency and changes its sign at the wings, while the FR signal is an odd function of the detuning between exciton resonance and probe optical frequency.

In Figs. 2(a) and 2(b), the measured dispersions of the FR and ellipticity signals are compared with the theoretical model. The signals are the superpositions of the exciton and trion contributions, as clearly seen at the higher energy side of the ellipticity signal measured for positive delays where it changes sign, Fig. 2(a). A similar trend is also observed for negative delays, Fig. 2(b), however the exciton contribution is less pronounced there.

We attribute the differences in the spectral behavior of the measured signals at positive and negative delays to the fact, that there are two subensembles of resident electrons, see e.g., Ref. 16. The electrons with stronger localization demonstrate longer spin relaxation time. They make a major contribution to the pump-probe signal at negative delays and modulate the signal at the trion frequency more efficiently as compared with the less localized carriers. The latter have shorter spin relaxation times so that their contribution is more pronounced in the signals at positive delays. This conclusion is supported by the observation that two Larmor frequencies which lie quite close to each other are detected for the long-lived signal, see below.

## IV. SPIN COHERENCE INITIALIZATION AND RESONANT SPIN AMPLIFICATION

The observation of electron spin polarization before the next pump pulse arrival indicates that the spin relaxation time is comparable or longer than the laser repetition period of 13.2 ns and that spin polarization may accumulate from pulse to pulse. The resonant spin amplification technique (RSA) allows us to extract the long spin relaxation times with high accuracy.[4] In this section, we discuss results of pump-probe Faraday rotation RSA experiments. We checked also that the ellipticity RSA data give the same spin relaxation times as the FR signals.
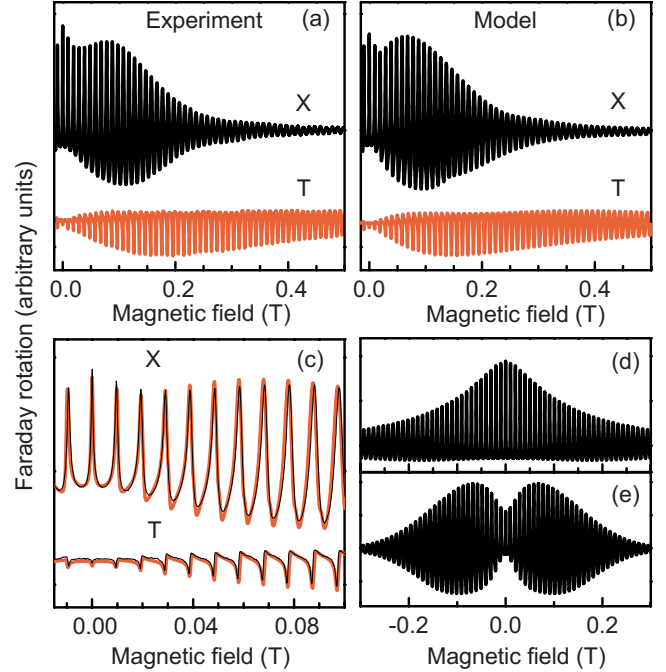


FIG. 4. (Color online) (a) and (c) RSA signals measured in degenerate pump/probe regime near the trion (1.4382 eV) and exciton (1.4395 eV) resonances at $T = 1.8$ K. Black curves in panel (c) are RSA experimental data and thick red (gray) curves are fits by Eq. (5). (b) Modeled RSA signals for the trion and exciton resonances. The two components in the theoretical RSA signal for exciton resonance due to spin orientation by exciton or trion absorption are shown separately in panels (d) and (e), respectively. Calculation parameters are: $T_s^e = 45$ ns and $\tau_r = 120$ ps, $\Theta = 0.1\pi$. For RSA on trion resonance: $|g_e| = 0.555$, $\Delta g_e = 0.002$, and $T_s^h = 2.5$ ns. For RSA on exciton resonance: (i) spin orientation by excitons $|g_e| = 0.535$ and $\Delta g_e = 0.003$; (ii) spin orientation by trions: $|g_e| = 0.550$, $\Delta g_e = 0.008$, and $T_s^h = 1.8$ ns.

Figure 4 shows RSA signals measured for degenerate pump/probe conditions near the trion and exciton resonance energies. The peaks in the RSA signals correspond to the spin precession frequencies which are commensurable with the laser repetition frequency. From the peak width the electron spin relaxation time $T_s^e$, which in this case corresponds to the spin dephasing time $T_{2,e}^*$ of the electron spin ensemble precessing about the magnetic field, can be evaluated.[4]

The spin amplification signals measured on the exciton and trion resonance qualitatively differ from each other, see Fig. 4(a). They deviate also from the typical RSA shape with decreasing peak amplitude and increasing peak width with increasing magnetic field, see Ref. 4 and Fig. 4(d). For the trion resonance the signal amplitude is strongly suppressed at zero magnetic field and the amplitude increases with growing field strength. For the exciton resonance the signal has a complicated shape, which results from a combination of the typical RSA signal from Fig. 4(d) and the trion batlike signal shown in Fig. 4(e) (see below).

The strong difference between the signals measured at the exciton and trion energies suggests that different mechanisms are involved in spin coherence generation. The strong suppression of the RSA signal at $B = 0$ for trion excitation and its

INITIALIZATION: Pump action, trion resonance

(a) $B = 0$, $T_h^s \gg \tau_r$



(b) $B = 0$, $T_h^s < \tau_r$
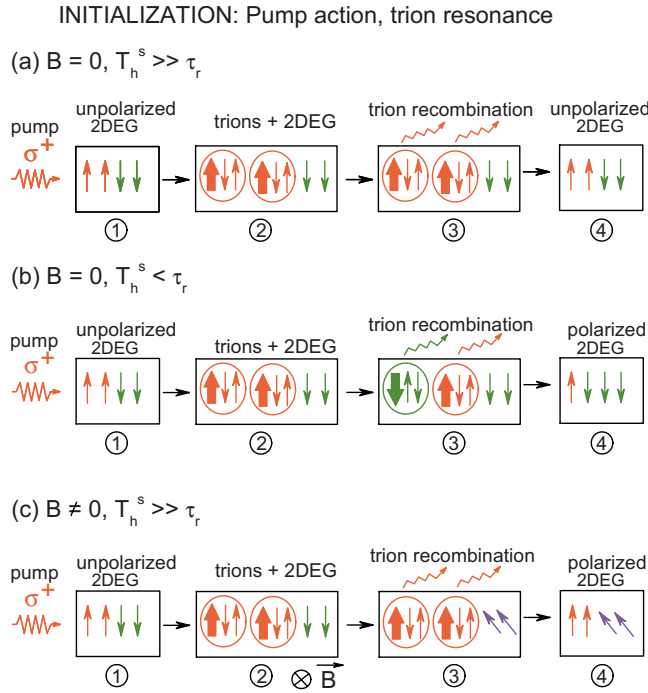


(c) $B \neq 0$, $T_h^s \gg \tau_r$



FIG. 5. (Color online) Spin orientation of resident electrons denoted as 2DEG (two-dimensional electron gas) for trion resonant excitation. The following four stages are shown: (1) unpolarized 2DEG before excitation; (2) result of action of a $\sigma^+$-polarized pump pulse, part of the resident electrons are bound to trions; (3) trions and resident electrons shortly before trion recombination; (4) 2DEG after trion recombination. Panels (a) and (b) show the situation for zero external magnetic field. (a) $T_h^s \gg \tau_r$, hole spin flip is absent and resident electrons stay unpolarized after trion recombination. (b) $T_h^s < \tau_r$, hole spin relaxes before trion decay and resident electrons become spin polarized. (c) Nonzero external magnetic field. Even in the absence of hole spin relaxation the resident electrons become polarized due to electron spin precession about magnetic field during trion lifetime.

batlike shape serves as direct evidence of the long spin relaxation time of the hole involved in the trion.[9] Indeed, in absence of the magnetic field the long-lived electron spin coherence at trion excitation can be generated only as much as the hole spin in trion flips, compare Figs. 5(a) and 5(b). If the hole spin relaxation time $T_s^h$ exceeds by far the trion recombination time, $\tau_r$, the resident electron left behind after trion recombination has the same spin as before and no long-living spin coherence for the resident electrons is generated, Fig. 5(a). With increase in the magnetic field the resident carrier spins and the spins of the electron returning from the trion are no longer parallel to each other and the RSA signal increases, see Fig. 5(c).

Interestingly, for excitation near exciton resonance (see Fig. 4) the signal is not suppressed at $B = 0$, which shows that electron spin coherence is efficiently excited even in the absence of electron spin rotation. The corresponding mechanism of resident electron spin coherence generation can be related with the spin flip-flop exchange scattering between a resident electron and a photoexcited electron in the exciton. In such a case the hole spin-flip is not needed: right after the electron flip-flop scattering an uncompensated resident elec-

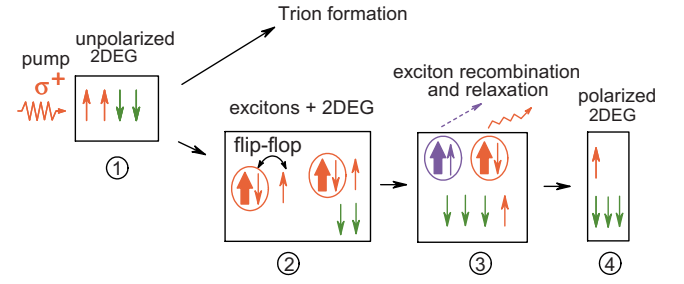INITIALIZATION: Pump action, exciton resonance



FIG. 6. (Color online) Spin orientation of resident electrons at exciton resonant excitation. Two possible scenarios are depicted: trion formation from the photocreated exciton and flip-flop scattering of an exciton with a resident electron. In this case the exciton is transformed into a dark state and the resident electrons become polarized after the dark state has decayed (shown by blue dashed arrow). Other notations are the same as in Fig. 5

tron spin appears (Fig. 6). This exchange scattering process may be the dominant channel for spin coherence generation at weak magnetic fields, while with increasing magnetic field the spin coherence generation via the trion state becomes more efficient. This results in the increase in the RSA amplitude for fields $B > 50$ mT, see Fig. 4(a).

The batlike trion signal shown in Fig. 4(a) can be modeled with good quantitative agreement, as seen from the comparison of the black and gray lines in Fig. 4(c), in the frame of the approach suggested in Ref. 9. An infinite sequence of pump pulses with repetition period $T_R$ creates an electron spin polarization periodic in time.[9,21] The electron spin polarization, $\tilde{s}_z$, shortly before pump pulse arrival is described by:[9,22]

$$\tilde{s}_z = \frac{1}{2}\left[\frac{K}{1 + ue^{-2T_R/T_s^e} - (1+u)\cos(\omega_e T_R)e^{-T_R/T_s^e} - K}\right],$$

$$K \equiv v[u\alpha e^{-T_R/T_s^e} - \alpha\cos(\omega_e T_R) - \beta\sin(\omega_e T_R)]e^{-T_R/T_s^e}.$$
(5)

Here $v \equiv \sin^2(\Theta/2)/2$, $u \equiv \cos(\Theta/2)$, $\Theta$ is pulse area, $\alpha \equiv 1 + \text{Re}[1/(\tau_r\Omega)]$, $\beta \equiv \text{Im}[1/(\tau_r\Omega)]$, $\Omega = 1/T_s^e - 1/\tau_T + i\omega_e$, $T_R$ is laser repetition period, $\omega_e = g_e\mu_B B/\hbar$ is the electron spin precession frequency, $\tau_r$ is the trion recombination time, $\tau_T = T_s^h\tau_r/(T_s^h + \tau_r)$ is the trion spin lifetime, $T_s^h$ is the hole spin relaxation time, and $T_s^e$ is the electron spin relaxation time.

The expression for a typical RSA contour which describes the contribution due to spin orientation by electron-exciton scattering can be found, for example, in the online materials to Ref. 6 as Eqs. (B4) and (B5) or in Ref. 17 as Eqs. (29) and (30). It is described by Eq. (5) with $K = v[ue^{-T_R/T_s^e} - \cos(\omega_e T_R)]e^{-T_R/T_s^e}$. An example of such signal is shown in Fig. 4(d).

In order to fit the complicated shape of the RSA signal measured at the exciton resonance we used a sum of contributions due to spin orientation by trion and by exciton. The gray line fit for the exciton in Fig. 4(c), results from two signals shown separately in Figs. 4(d) and 4(e). These two

contributions have not only different shapes but also slightly different electron *g* factors and spreads of *g* factors, as given in the figure caption. The presence of two Larmor frequencies for the signals measured at exciton resonance can be related with the coexistence of two electron subensembles with different degree of localization and corresponding variation of the *g* factor with electron energy.[23] The slight difference of *g* factors obtained from RSA and time-resolved FR signal at trion resonance can be related with the nuclear effects and is not important for the purposes of the present study. The weaker localized carriers, which have a stronger impact on the exciton resonance, have a smaller *g* factor and a smaller dispersion.

It is worth mentioning that for exciton resonant excitation higher energy trions can be formed as compared to the case of trion resonant excitation. These trions can be weaker localized so that they demonstrate short hole spin relaxation times, resulting in efficient spin coherence generation for resident electrons at *B*=0. The contribution of such a channel can be described by the conventional RSA shape shown in Fig. 4(d). However, in the studied sample the role of the exciton under these experimental conditions dominated over the possible trion contribution. There are two arguments for this conclusion: (i) the spectral dependence of amplitude of the RSA signal with usual shape [Fig. 4(d)] has maximum at exciton pumping and (ii) this amplitude increases with increasing of pump power and disappears with decrease in pump power. It allows us to conclude that the main contribution to the RSA signal with shape shown in Fig. 4(d) is due to electron spins polarized by electron-exciton scattering or due to fast spin relaxation of hole in the resonantly excited exciton.

## V. LOW-TEMPERATURE SPIN DYNAMICS

We turn now to the evolution of the spin dynamics of electrons and holes and in particular to the mechanisms providing carrier spin relaxation at extremely low temperatures down to 430 mK. We focus on the Faraday rotation RSA signals measured at the trion resonance, where the hole spin dynamics is most pronounced. Figure 7 shows RSA signals measured at the trion resonance energy for various temperatures. We fit the experimental RSA spectra from Fig. 7 by Eq. (5) and get very good agreement in all cases. The *g* factors and spin relaxation times determined in that way are given in the figure caption.

The electron and hole spin relaxation times measured at different temperatures are collected in Fig. 8. The data for temperatures below 15 K were determined from RSA spectra and for higher temperatures, at which the RSA signals vanish, we fit the decay of the FR signals at positive delays. The data in the temperature range 0.43–10 K have been measured using the $^3$He insert and in the temperature range 1.6–80 K in a $^4$He insert. The two temperature ranges were chosen to have overlap, in order to confirm consistency of the data.

The temperature dependencies of spin relaxation times for electrons and holes are qualitatively similar. The times almost do not change at very low temperatures, which show that the spin dynamics in these regimes are controlled by
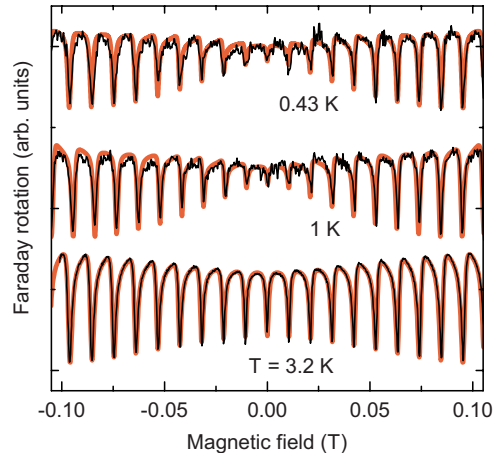


FIG. 7. (Color online) RSA signals measured by degenerate pump-probe Faraday rotation at the trion resonance for various temperatures. Black curves are experimental data and thick red (gray) curves are fits by Eq. (5). Calculation parameters are: $|g_e|$=0.555, $T_s^e$=45 ns, and $\Theta$=0.1$\pi$ for $T$=0.43 K: $T_s^h$=2 ns and $\tau_r$=200 ps; for $T$=1 K: $T_s^h$=2 ns and $\tau_r$=200 ps; for $T$=3.2 K: $T_s^h$=0.6 ns and $\tau_r$=120 ps.

temperature independent mechanisms. At elevated temperatures the times drop by more than an order of magnitude. As can be seen from the solid lines in Fig. 8 these behaviors can be well fitted by the following function describing thermal activation from the ground state with a long relaxation time to an excited state with a shorter relaxation time
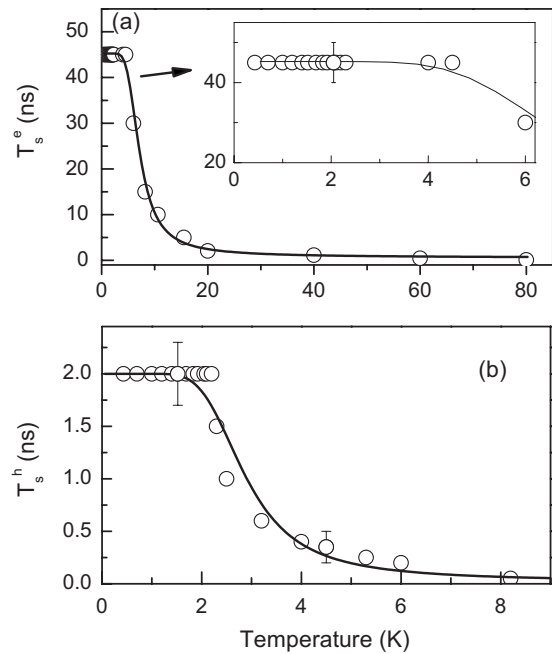


FIG. 8. Temperature dependencies of electron (a) and hole (b) spin relaxation times in an (In,Ga)As/GaAs QW. Symbols are experimental data and lines are fits with Eq. (6) using the following parameters: $T_0^e$=45 ns, $T_{exc}^e$=0.5 ns, and $\Delta E_e$=3 meV for electrons in panel (a), and $T_0^h$=2 ns, $T_{exc}^h$=10 ps, and $\Delta E_h$=1.4 meV for holes in panel (b).

$$\frac{1}{T_s^{e(h)}} = \frac{1}{T_0^{e(h)}} + \frac{1}{T_{exc}^{e(h)}}\exp\left(-\frac{\Delta E_{e(h)}}{k_B T}\right). \quad (6)$$

Here $T_0^{e(h)}$ are the spin relaxation times in the electron (hole) ground states, $T_{exc}^{e(h)}$ are constants characterizing the transitions between the ground and excited states which depend on the electron-phonon interaction, $\Delta E_{e(h)}$ are the characteristic activation energies, and $k_B$ is the Boltzmann constant. One should note that this approach is rather simplified and gives physically feasible values of the fitting parameters for a relatively narrow temperature range. Therefore, it should be valid for holes in a temperature range not exceeding 8 K, while for electrons, for which experimental data have been recorded up to 80 K, additional mechanisms may cause the temperature dependencies of $T_{exc}^e$ and $\Delta E_e$ so that more elaborated approach may be required.

The electron spin relaxation time, $T_s^e$, is constant in the temperature range from 0.43 to 4.5 K at an extremely large value of 45 ns, see insert in Fig. 8(a). At these temperatures the resident electrons are localized and their spin relaxation is provided by the hyperfine interaction with the nuclei spins, which is almost temperature independent. At temperatures above 5 K the resident electrons are thermally activated and the Dyakonov-Perel relaxation mechanism[1] which is very efficient for free electrons starts to act. As a result the relaxation time drops to 1.1 ns at 40 K and further down to 110 ps at 80 K. Such a behavior is typical for $n$-doped QWs with a diluted concentration of the resident electrons.[8,9,15]

Let us turn now to the temperature dependence of the hole spin relaxation time, $T_s^h$, in Fig. 8(b). Below 2.2 K $T_s^h$ saturates at a value of 2 ns. At the moment it is not clear to us what relaxation mechanism is controlling the hole spin dynamics in the range 0.43–2.2 K. Most probably it is due to the admixture of the light-hole to the heavy-hole states, enhancing strongly the possibility for spin-flip scattering.

The hyperfine interaction with the nuclei is significantly weaker for the holes than for the electrons. This has been confirmed by the recent report on ultralong hole spin relaxation with about 70 ns relaxation time, measured in the range 0.4–1.2 K for a $p$-doped 4 nm GaAs/Al$_{0.3}$Ga$_{0.7}$As QW.[14] Our experimental situation differs from the one in $p$-doped samples with resident holes, as in $n$-doped samples we detect the spin dynamics of photogenerated holes bound in negatively charged trions. However, in the trion ground state, which is a singlet state, the two electrons have antiparallel spin orientations and flip-flop electron-hole process are not possible without exciting the trion complex into a triplet state, which requires an energy similar to the trion binding energy of 1.4 meV. In fact this energy is in very good agreement with the activation energy $\Delta E_h = 1.4$ meV, which has been obtained from fitting the experimental data in Fig. 8(b) by Eq. (6). Therefore, we suggest that the strong decrease in the hole spin relaxation time at temperatures above 2.2 K is either due to trion thermal dissociation, which excites the hole into the continuum of free states with a strong spin-orbit interaction leading to a fast spin relaxation or due to flip-flop process involving the trion triplet state.

In conclusion, the carrier spin dynamics in an $n$-doped (In,Ga)As/GaAs QW have been studied by the resonant spin amplification technique at very low lattice temperatures down to 0.43 K. Carrier localization leads to a saturation of the spin relaxation times at 45 ns for electrons below 4.5 K and at 2 ns for holes below 2.3 K. Also the spectral dependencies of the Faraday rotation and ellipticity signals have been studied experimentally around the trion and exciton resonances. The mechanisms responsible for spin polarization of the resident electrons under resonant pumping into the trion and exciton resonances have been discussed.

[1] *Spin Physics in Semiconductors*, edited by M. I. Dyakonov (Springer-Verlag, Berlin, 2008).

[2] *Semiconductor Spintronics and Quantum Computation*, edited by D. D. Awschalom, D. Loss, and N. Samarth (Springer-Verlag, Berlin, 2002).

[3] *Semiconductor Quantum Bits*, edited by F. Henneberger and O. Benson (Pan Stanford, Singapore, 2009).

[4] J. M. Kikkawa and D. D. Awschalom, Phys. Rev. Lett. **80**, 4313 (1998).

[5] R. I. Dzhioev, B. P. Zakharchenya, V. L. Korenev, and M. N. Stepanova, Fiz. Tverd. Tela (Leningrad) **39**, 1975 (1997) [Sov. Phys. Solid State **39**, 1765 (1997)].

[6] A. Greilich, D. R. Yakovlev, A. Shabaev, Al. L. Efros, I. A. Yugova, R. Oulton, V. Stavarache, D. Reuter, A. Wieck, and M.

Bayer, Science **313**, 341 (2006).

[7] S. A. Crooker, J. Brandt, C. Sandfort, A. Greilich, D. R. Yakovlev, D. Reuter, A. D. Wieck, and M. Bayer, Phys. Rev. Lett. **104**, 036601 (2010).

[8] E. A. Zhukov, D. R. Yakovlev, M. Bayer, G. Karczewski, T. Wojtowicz, and J. Kossut, Phys. Status Solidi B **243**, 878 (2006).

[9] I. A. Yugova, A. A. Sokolova, D. R. Yakovlev, A. Greilich, D. Reuter, A. D. Wieck, and M. Bayer, Phys. Rev. Lett. **102**, 167402 (2009).

[10] X. Marie, T. Amand, P. Le Jeune, M. Paillard, P. Renucci, L. E. Golub, V. D. Dymnikov, and E. L. Ivchenko, Phys. Rev. B **60**, 5811 (1999).

[11] B. Baylac, T. Amand, X. Marie, B. Dareys, M. Brousseau, G.

Bacquet, and V. Thierry-Mieg, Solid State Commun. **93**, 57 (1995).

[12] M. Syperek, D. R. Yakovlev, A. Greilich, J. Misiewicz, M. Bayer, D. Reuter, and A. D. Wieck, Phys. Rev. Lett. **99**, 187401 (2007).

[13] M. Kugler, T. Andlauer, T. Korn, A. Wagner, S. Fehringer, R. Schulz, M. Kubova, C. Gerl, D. Schuh, W. Wegscheider, P. Vogl, and C. Schüller, Phys. Rev. B **80**, 035325 (2009).

[14] T. Korn, M. Kugler, M. Griesbeck, R. Schulz, A. Wagner, M. Kubova, C. Gerl, D. Schuh, W. Wegscheider, and C. Schüller, arXiv:0909.3711 (unpublished).

[15] I. Ya. Gerlovin, Yu. P. Efimov, Yu. K. Dolgikh, S. A. Eliseev, V. V. Ovsyankin, V. V. Petrov, R. V. Cherbunin, I. V. Ignatiev, I. A. Yugova, L. V. Fokina, A. Greilich, D. R. Yakovlev, and M. Bayer, Phys. Rev. B **75**, 115330 (2007).

[16] E. A. Zhukov, D. R. Yakovlev, M. Bayer, M. M. Glazov, E. L. Ivchenko, G. Karczewski, T. Wojtowicz, and J. Kossut, Phys. Rev. B **76**, 205310 (2007).

[17] I. A. Yugova, M. M. Glazov, E. L. Ivchenko, and Al. L. Efros, Phys. Rev. B **80**, 104436 (2009).

[18] The inhomogeneous broadening of exciton and trion resonances caused by the localization of charge carriers and their complexes on quantum well structure imperfections can be taken into account by convolution of Eq. (2) with the proper distribution of resonant frequencies. Effectively, such an averaging leads to an increase in the constants $\Gamma_i$ describing nonradiative damping. Introduction of two independent parameters for each resonance: one describing the nonradiative damping and other describing inhomogeneous broadening for, e.g., Gaussian distribution of resonance energies, leads to even better agreement between line shapes in experiment and theory, however, we decided to keep the smallest possible fitting parameters which allow to obtain the agreement.

[19] E. L. Ivchenko, *Optical Spectroscopy of Semiconductor Nanostructures* (Alpha Science, Harrow, UK, 2005).

[20] G. V. Astakhov, V. P. Kochereshko, D. R. Yakovlev, W. Ossau, J. Nürnberger, W. Faschinger, and G. Landwehr, Phys. Rev. B **62**, 10345 (2000). The values introduced in this paper: $A$ is the area of QW layer and $A_T$ is the trion area. They are in the following relation with the $\alpha_T$ value from the present paper: $\alpha_T = A_T/A$.

[21] A. Shabaev, Al. L. Efros, D. Gammon, and I. A. Merkulov, Phys. Rev. B **68**, 201305(R) (2003).

[22] In Eqs. (5) and (6) of Ref. 9 factor $\exp(-T_R/T_s^e)$ and minus at last term of denominator were lost.

[23] I. A. Yugova, A. Greilich, D. R. Yakovlev, A. A. Kiselev, M. Bayer, V. V. Petrov, Y. K. Dolgikh, D. Reuter, and A. D. Wieck, Phys. Rev. B **75**, 245302 (2007).